NJC

PAPER

Cite this: *New J. Chem.*, 2025, **49**, 5529

Cetyltrimethylammonium bromide modified magnetic apricot shells for removing Congo red dye and an artificial neural network model

Akinshola Olabamiji Akinola, Eswaran Prabakaran, Krishna Govender and Kriveshini Pillay *

This study focused on the synthesis of a cetyltrimethylammonium bromide-modified magnetic (Fe_3O_4@Ap/CTAB) nanocomposite from apricot shells and utilised an artificial neural network (ANN) to model the process parameters for removing Congo red (CR) dye from the aqueous environment. The as-prepared magnetic nanocomposite was characterised using various instrumental techniques such as Fourier Transform infrared spectroscopy (FT-IR), scanning electron microscopy (SEM), energy dispersive X-ray analysis (EDX), transmission electron microscopy (TEM), X-ray diffraction spectroscopy (XRD) and Brunauer–Emmett–Teller (BET) analysis. The nanocomposites showed sheet-like clusters of AS with dark particles of Fe_3O_4 on the surface. The point of zero charge (pH_{pzc}) was found to be 8.04, while the surface area and the pore volume were 18.7842 $m^2\ g^{-1}$ and 0.089736 $cm^3\ g^{-1}$, respectively. The Fe_3O_4@Ap/CTAB nanocomposite was used as an adsorbent for the removal of Congo red (CR) dye under different conditions. The optimal sorption conditions achieved the highest capacity of 37.175 mg g^{-1} at 25 °C and 44.053 mg g^{-1} at 45 °C, at pH 6.5, with a dosage of 50 mg and a concentration of 22.3 mg L^{-1} in 4 hours. The nanocomposite achieved a 95.77% removal efficiency from real wastewater after shaking for 180 minutes at 25 °C under natural wastewater conditions. The data conformed mostly to the pseudo-second-order kinetic model and Langmuir isotherm, with the thermodynamic studies indicating a favourable, endothermic and spontaneous process with an ΔH° value of +27.193 kJ mol^{-1}. The adsorbent efficiently sequestered the dye from the wastewater *via* physical adsorption and electrostatic attractions. A multi-layer 'feed-forward neural network', comprising 5 input parameters, a hidden layer, and an output parameter, was employed to predict CR removal efficiency. The performance of the network, evaluated by the coefficient of regression (R^2), mean squared error, average percentage error, and mean absolute error, demonstrated a high R^2 value of 0.9587. The minimal relative percentage error between the predicted and the test data confirms the ANN's effectiveness in capturing the non-linear behaviour of CR removal. This model of ANN can be employed for the prediction and optimisation of the adsorption process parameters for maximising CR removal using Fe_3O_4@Ap/CTAB, thereby aiding in the provision of pure water.

Received 16th November 2024,
Accepted 19th February 2025

DOI: 10.1039/d4nj04953e

rsc.li/njc

Introduction

The increasing development of industry has made the pollution of water a global concern. Surface and underground water bodies have become the ultimate recipients of the majority of industrial effluents and chemical residues emanating from industrial practices. These effluents from industries and agrarian practices contain organic and inorganic contaminants.[1] Releasing these hazardous substances into the environment constitutes humungous problems for the ecosystem. Due to extensive anthropogenic practices, toxic metals, dyes, pesticides and pharmaceuticals, which represent the significant classes of organic and inorganic priority contaminants in water, navigate their way into the primary surface and subsurface water in villages and cities.[2,3]

Synthetic dyes, apart from their interference with the aesthetic value of water, have also been found to be detrimental to human health. The contamination of surface and underground water by dyes through various human and natural activities has become a global concern from diverse quarters in developed and developing countries. These organic pollutants pose serious threats to aquatic life and humans due to their non-biodegradability and accumulation in the ecosystem if inappropriately handled.[4] Textile, dye and printing industries utilise a lot of water and produce huge amounts of wastewater with dyes, which are mainly organic. When these wastewaters are inappropriately

---

Department of Chemical Sciences, University of Johannesburg, Johannesburg, South Africa. E-mail: kriveshinip@uj.ac.za

treated and released into the environment, they pose an unquantifiable threat to land and water organisms. Dyes from textile industries, such as Congo red (CR) which is anionic, pose many health hazards, including damage to the human brain, reproductive systems, kidneys, nervous system and liver.[5] CR, a direct anionic diazo dye which is stable and mostly non-biodegradable, is one of the major contaminants in water from the dye-utilising industries. CR has been found to present several dangers to living organisms upon exposure. These include acute toxicity to yeast, bacteria, protozoa, algae and other microorganisms. It has also been reported to likely cause cancer, mutations, genotoxicity, neurotoxicity and hematotoxicity.[6] Due to these lethal effects, CR must be sequestered from wastewater before its release into the environment. The contamination of underground water has caused widespread concern as it has reduced the quality of drinking water in the world, which severely restricts the attainment of the sixth sustainable development goal of providing clean water and sanitation to all humanity by 2030.[7,8] Therefore, it is fundamentally essential to ensure the treatment of wastewater in order to satisfy the legislated safety measures before being discharged into the aquatic environment.

Over time, several removal approaches for the removal of dyes from water have been studied due to their persistent nature and inefficient removal by biodegradation. Numerous methods, such as ultrafiltration, photocatalysis, coagulation, adsorption, nanofiltration, and so on, have been exploited for sequestering Congo red from water.[9] Out of all these removal techniques, adsorption has proven to be highly beneficial for a number of reasons, including low energy requirement, selectivity, efficiency, lower cost, *etc.* Due to its comparatively lower cost, availability of a large range of adsorbents, effective treatment with no production of harmful by-products, and ease of handling, adsorption has the greatest appeal and potential.[10,11] Commercially accessible and high-quality activated carbon (AC) has been successful in removing several contaminants from water as an adsorbent.[12] Even so, the high cost of AC has rendered it utterly uneconomical for usage on an industrial scale, necessitating the search for affordable, renewable, but effective substitute adsorbents for remediating water and wastewater. Hence, cheaper absorbents are required to remove CR from water samples efficiently.

The separation of Congo red through adsorption from water has reportedly been accomplished using a variety of agricultural wastes and natural materials, including *Antigonon leptopus* leaf powder,[9] *Grevillea robust* composite,[6] water hyacinth,[13] *Aloe vera* shells,[14] pine cones,[15] coir pith, rice husks and banana peels.[16]

Apricot is a member of the *Rosaceae* family of plants and is mostly grown in Africa, Asia, and Europe. A significant number of apricot shells are created during the processing of the seeds, and these are either thrown away as agricultural waste or used as a supplement to increase soil fertility.[17,18] Apricot waste has been employed as the least expensive adsorbent to remove dyes and heavy metals.[19] Apricot wastes were utilised to remove dyes such as crystal violet, malachite green, and methylene blue from aqueous solutions,[20] while the stones (seeds) were used for the removal of astrazone yellow,[21] astrazone black,[22] and Congo red.[23,24] Notwithstanding, the use of apricot stone shells is yet to be fully explored for the removal of CR.

However, the use of unmodified adsorbents often leads to suboptimal performance due to limitations in adsorption capacity, efficiency, and separation after use.[25] This is evident in previous studies.[23,24] Recently, because of their remarkable qualities, which include a large surface area, a large number of reactive atoms, excellent mechanical and thermal stability, and a large number of reactive surface sites, nano-adsorbents have attracted a lot of attention. Numerous metal-based nanoscale adsorbents have shown exceptional removal effectiveness for poisonous dyes from aqueous solutions, including ZnO/$Zn(OH)_2$, ZnO nanorods, ZnS, Cu-doped ZnS, Mn-doped Fe_3O_4, and SnO_2 nanoparticles.[26] Traditional adsorbents can be challenging to separate from aqueous solutions and are prone to agglomeration during the adsorption process, hindering their practical applications. For these challenges to be surmounted, researchers are increasingly exploring the potential of magnetic nanomaterials. These materials offer a unique advantage due to their inherent magnetic properties, enabling rapid and efficient separation from liquids using an external magnetic field. This reusability significantly enhances their practicality.[27] Notwithstanding, bare magnetic nanomaterials, while promising, face a problem: their high surface energy often leads to agglomeration. Surface modification has emerged as a common approach to address this issue, improving nanoparticle dispersion. However, there is currently very little research on the exploration of apricot stone shells (ASs), an abundantly available agricultural waste, as a viable precursor for synthesising a novel magnetic nanocomposite for the removal of organic pollutants from water.[28] In this sense, pristine ASs are hard to separate from water, regenerate and reuse. Given these drawbacks, ASs have been incorporated with Fe_3O_4 to enhance its magnetic separation in this study. This modification can sometimes limit adsorption capacity due to the relatively thin functional shell layer coating the magnetic core. This research therefore adopts an alternative strategy that involves the creation of composite materials combining magnetic components with porous carbon structures and enhancing their dispersion and efficiency using CTAB, a positively charged surfactant, to improve their surface area, dispersibility, adsorption capabilities, separation, regeneration, and reusability for the removal of CR. AS was employed as the base material, offering a high surface area and pore volume, thereby significantly enhancing the composite's adsorption capacity for a wide range of pollutants, such as CR dye. Fe_3O_4 provides magnetic properties, enabling easy separation of the composite from solutions using an external magnetic field and also contributing to the composite's adsorption capacity. CTAB in the Fe_3O_4@Ap/CTAB composite primarily functions as a surface modifier, enhancing the dispersion and introducing a positive surface charge. This modification is beneficial for improving the adsorption of the anionic dye. Since it is a positively charged surfactant, CTAB adsorbs onto the surface of the composite thereby enhancing the dispersion of the nanocomposite, reducing aggregation and increasing the effective surface area for adsorption. Furthermore, CTAB introduces a positive charge from the quaternary ammonium group on the surface of the composite, which significantly helps to expedite the adsorption of the anionic CR dye. This CTAB-modified magnetic composite therefore offers a larger surface area, thereby effectively mitigating agglomeration while potentially enhancing the adsorption of the anionic CR dye and separation efficiency.

Modelling adsorption processes benefit significantly from using artificial neural networks (ANNs). ANNs are well suited for handling complex adsorption data since they are excellent at capturing non-linear connections. They can adapt to various conditions without making assumptions about adsorption mechanisms because of their data-driven approach.[29] ANN can process a variety of data formats, including structural data, and automatically extract the necessary features, thereby eliminating the need for manual feature engineering. They offer good prediction power for novel adsorption conditions and are resilient to noisy data. ANNs scale well, benefit from parallel processing, and perform well when applied to new data. For effective and generalisable ANN model training, it is essential to have access to a sizable and diverse data collection.[30] Artificial intelligence (AI) techniques have been employed to provide solutions to difficult problems. Artificial neural networks (ANNs), which process data by imitating the human brain system, are an AI method used for solving complex problems.[31] ANN has therefore been employed to predict the efficacy of the adsorptive removal process. A number of studies have used ANN to predict the efficiency or the adsorptive capacities of different adsorbents in removing diverse forms of pollutants from water. The reported studies include the employment of ANN to predict the efficiency of the removal of copper(II) using pumice,[32] electrocoagulation for the decolorisation of Basic Yellow,[33] removal of lead(II) with rice husks,[34] and with *Prosopis juliflora*.[35] However, there is currently no available report on the use of ANNs for modelling the adsorption efficiency of the synthesised composite sorbents prepared from AS. Pristine AS is difficult to separate from aqueous solutions and tends to agglomerate during use, limiting their practicality. The incorporation of magnetic nanomaterials allows for quick and efficient separation using external magnetic fields, thereby enhancing reusability. However, bare magnetic nanomaterials are prone to agglomeration due to their high surface energy. Thus, the surfactant CTAB is introduced as a strategy to improve their dispersion to overcome this challenge, as well as increase the positively charged groups on the surface of the Fe_3O_4@Ap/CTAB nanocomposites for the enhanced uptake of the negatively charged CR dye molecules. Thus, this study utilised apricot stone shells to synthesise a novel cetyltrimethylammonium bromide (CTAB) modified magnetic composite as a substitute sorbent, offering a larger surface area, effectively mitigating agglomeration, while potentially enhancing the adsorption of anionic CR dye and separation efficiency in treating water and wastewater containing CR. Furthermore, the adsorption capacity of the dye within a minimal timeframe was investigated while maintaining a near-neutral pH during the process. Various experimental parameters, such as solution pH, adsorbent dosage, contact time, and the initial CR dye concentration, were systematically varied to evaluate their impact on dye removal efficiency. Additionally, the kinetics and the thermodynamics of the process were studied; the reusability of the composite was evaluated, and an artificial neural network (ANN) model was developed using Python programming to predict the adsorption efficiency. The efficacy of the Fe_3O_4@Ap/CTAB composite was also evaluated in an actual wastewater sample spiked with CR dye.

Materials and methods

Analytical grade reagents were utilised in this study. Sigma-Aldrich supplied iron(II) chloride tetrahydrate ($FeCl_2 \cdot 4H_2O$) (99%), cetyltrimethylammonium bromide (CTAB) (99%), hydrochloric acid (HCl) (37%) and sodium hydroxide (NaOH) (>98%).

Apricot stones were collected from the Johannesburg fresh fruit market, City-deep, South Africa. The stones were washed with tap water several times, then dried, and the shells were separated. The shells were pulverised into particle sizes of 10–53 μm and stored for the synthesis of the composite.

Synthesis of the magnetic composite

The pulverised apricot stone shell (AS) was combined with magnetic nanoparticles using iron(II) chloride tetrahydrate ($FeCl_2 \cdot 4H_2O$) *via* the following steps. 2.68 g of $FeCl_2 \cdot 4H_2O$ was dissolved in 80 mL of a solution of 1 M hydrochloric acid (HCl) at 70 °C and stirred for 10 minutes. 2.0 g of powdered AS was stirred into the solution for 50 minutes. The resulting mixture was adjusted to pH 10.4 with a dropwise addition of 3 M aqueous solution of NaOH. The resulting final black mixture was then sonicated for 30 minutes. This was separated and washed several times with deionised water and ethanol. The composite was dried at 60 °C for 14 hours and then carbonised at 180 °C for 18 hours. The mechanism for the formation of Fe_3O_4 is given below.

$FeCl_2 \cdot 4H_2O$ dissolves in HCl to give Fe^{2+} ions

$$FeCl_2 \cdot 4H_2O \xrightarrow{HCl_{(aq)}} Fe^{2+} + 2Cl^- + 4H_2O$$

Part of the Fe^{2+} oxidised to Fe^{3+} in the presence of O_2 and AS

$$Fe^{2+} + 4H^+ + O_2 \xrightarrow{70\ ^\circ C;\ AS} Fe^{3+} + 2Cl^- + 2H_2O$$

On addition of NaOH, Fe^{2+} and Fe^{3+} are coprecipitated with the apricot shell (Ap) as $Fe(OH)_2$/Ap and $Fe(OH)_3$/Ap.

$$Fe^{2+} + Fe^{3+} + Ap + 5OH^- \rightarrow Fe(OH)_2/Ap + Fe(OH)_3/Ap$$

$$2Fe(OH)_3/AS + Fe(OH)_2/AS \xrightarrow{pH=10.4;\ 70^\circ C;\ stir} Fe_3O_4@Ap + 4H_2O$$

NaCl and water are formed as the by-products from the addition of NaOH to $FeCl_2 \cdot 4H_2O$ and the oxidation of Fe^{2+} to Fe^{3+}, respectively.

Modification of the composite with CTAB

The synthesised magnetic iron oxide apricot stone shell (Fe_3O_4@Ap) was further modified with CTAB in a ratio of 1 : 1 (w/w) to enhance its affinity and uptake for the target pollutant. The preparation of aqueous CTAB was conducted by placing 2 g of the compound in 200 mL of deionised H_2O at room temperature with thorough stirring. 2 g of the Fe_3O_4@Ap was added to this solution. This was shaken for 24 hours at 130 rpm and 30 °C. The modified composite (Fe_3O_4@Ap/CTAB) was separated, washed and dried for 14 hours at 60 °C in a vacuum oven. This was stored in airtight glass vials for characterisation and further application. This process is shown in Scheme 1.

Characterisation of the nanocomposite

The Fe_3O_4@Ap/CTAB nanocomposite was characterised using various instrumental techniques. The physical and chemical attributes of both raw apricot stone shells and the synthesised nanocomposite were analysed using a blend of methods *viz.*: X-ray diffraction (using XRD, Rigagu Ultima IV, Japan), thermal gravimetric analysis (TGA) on a TGA Q500 (TA Instruments, USA), Fourier-transform infrared spectroscopy (FTIR), energy dispersive X-ray spectroscopy (EDX), scanning electron microscopy (SEM), transmission electron microscopy (TEM), and Brunauer–Emmett–Teller (BET) analysis. These advanced analytical methods offered insightful information about the successful synthesis of the nanocomposite and its potential as an efficient adsorbent.

Similarly, the surface charge of the Fe_3O_4@Ap/CTAB was determined at various pH values (2 to 13). The pH shift was plotted *versus* the initial pH to obtain the pH at which there is a neutral charge on the surface (pH_{pzc}). The initial pH was prepared by adding 0.1 M HCl/NaOH to a mixture containing 175 mg of Fe_3O_4@Ap/CTAB in 350 mL 0.1 M aqueous solution of NaCl. This was agitated for 24 hours to obtain the final pH.[4,36] The results are shown in Fig. 5(b).

Procedures of adsorption

Standard batch adsorption procedures were employed to assess the effectiveness of the synthesised magnetic nanocomposite in removing CR. The influences of various adsorption features, including initial concentration of CR (5–50 mg L^{-1}), time of agitation (1–300 minutes), quantity of adsorbent (10–200 mg), temperature (298–318 K) and pH (1–11) were systematically investigated at 180 rpm in a water bath shaker. The drawn aliquots were separated with a magnetic bar and analysed at 498 nm on a UV spectrophotometer (Agilent Cary 60, version 2.0). Eqn (1) below was utilised to determine the removal efficiency (%).

$$\%\ \text{Removal} = \frac{(C_o - C_e)}{C_o} \times 100 \qquad (1)$$

where C_o and C_e are, respectively, the starting and equilibrium concentrations of CR (mg L^{-1}).

Studies on the isotherm were executed to analyse the adsorption process at equilibrium, providing insights into the properties, efficiency, and mechanisms of the sorbents.

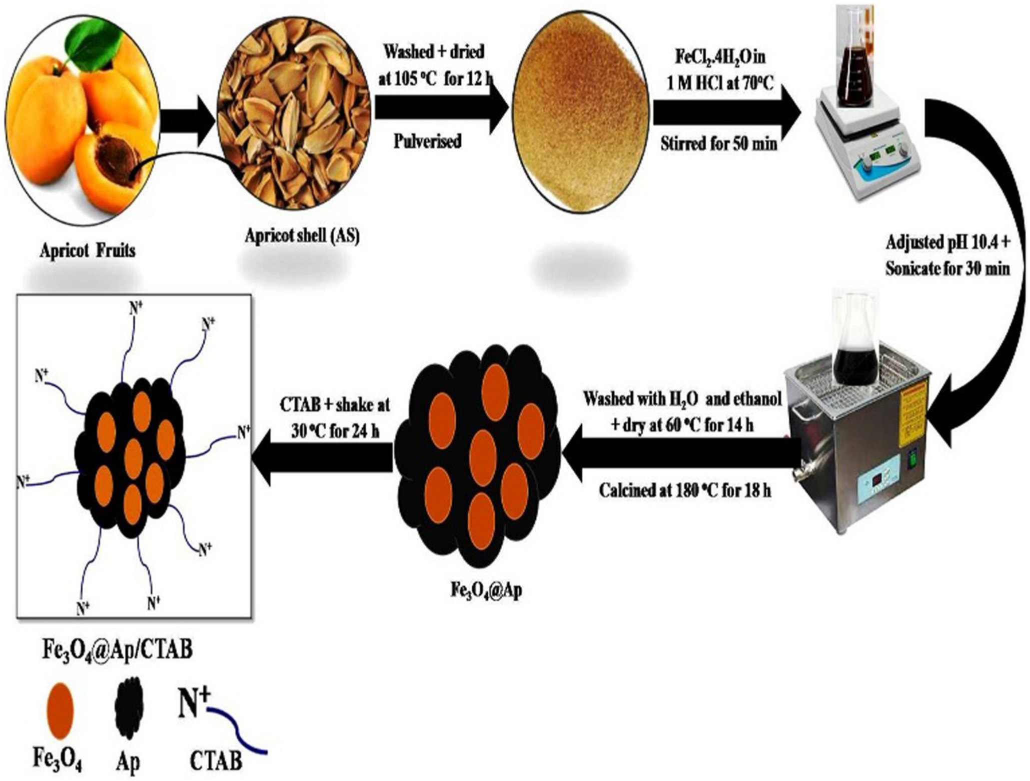

Scheme 1 Synthesis of the Fe_3O_4@Ap/CTAB nanocomposite.

The obtained data were fitted to Langmuir, Temkin and Freundlich isotherm models to determine the most appropriate model governing the sorption processes.[37–39] The efficacy of the Fe_3O_4@Ap/CTAB was then evaluated on an actual wastewater sample spiked with CR dye. All procedures were repeated three times to ensure the precision and accuracy of the results. The standard deviation of the obtained data was below 5%.

Development of an artificial neural network (ANN) optimal model

Various ANN architectures were examined to determine the optimum model to predict CR removal efficiency. Python neural network toolbox was explored using the experimental data obtained. The pH, time of agitation, initial concentration of CR, adsorbent dose, and temperature of the reaction were the input values (independent variables). The percentage removal of CR was the output (dependent variable). This was grouped into two sets: training (80%) and test (20%).

The adsorption model's neural network was built in a feed-forward approach with the multi-layer perceptron regressor (MLPRegressor) in Python's Scikit-learn library (Python 3.10.12 with tensorflow version 2.15.0). This comprised a 'feed-forward neural network' with complete connectivity containing input features (5), a single hidden layer (containing 100 neurons) and an output layer. A parameter grid search was conducted for hyperparameter tuning using a single or several concealed layers with various numbers of neurons (from 2 to 100). Three different activations functions: 'hyperbolic tangent' (Tanh), 'rectified linear unit' (ReLU), and sigmoid, with three optimisers: stochastic gradient descent (SGD), 'adaptive moment estimation' (Adam), and 'Limited-memory Broyden–Fletcher–Goldfarb–Shanno' (LBFGS) were explored for the parameter tuning at alpha values of 0.0001, 0.001 and 0.01; using the adaptive and constant learning rates. An instance of MLP Regression was created with maximum iterations of 1000 and a random state of 42. The best model with its hyperparameters was obtained. The best model was trained using the entire training dataset and subsequently used to forecast the efficiency of adsorption. The model was evaluated using mean absolute error (MAE), mean square error (MSE) and R^2.[31,35] The prediction was then compared with the actual experimental results.

Results and discussion

Characterisation of the nanocomposite

FTIR analysis. The functional groups on pristine AS and the Fe_3O_4@Ap/CTAB nanocomposite were studied using Fourier-transformed infrared (FTIR) spectroscopy, with the corresponding results presented in Fig. 1. The bands at 3435 cm^{-1}, 2938 cm^{-1}, 2872 cm^{-1}, 2028 cm^{-1}, 1637 cm^{-1}, 1264 cm^{-1}, 1050 cm^{-1}, 889 cm^{-1}, and 824 cm^{-1}, which are respectively allocated to the –OH stretching of alcohols, C–H stretching of alkenes, C–H stretching of alkanes, stretching vibration of C=O in ketone groups,[40] C=C of alkenes, asymmetric C–C–O aromatics, C–O cellulose and hemicelluloses, –CH cellulose, and –CH cellulose in the raw AS, were found to have shifted accordingly in Fe_3O_4@Ap/CTAB to 3416 cm^{-1}, 2920 cm^{-1}, 2843 cm^{-1}, 2022 cm^{-1}, 1633 cm^{-1}, 1271 cm^{-1}, 1018 cm^{-1}, 949 cm^{-1}, and 829 cm^{-1}. The bands that disappeared from the raw AS spectrum include 1732 cm^{-1} apportioned to –C=O hemicellulose, 1587 cm^{-1} assigned to C=C of lignin, 1510 cm^{-1} ascribed to C–C aromatics, 1460 cm^{-1} assigned to C–H of deformation in lignin, 1376 cm^{-1} allocated to the C–H of cellulose and hemicellulose, 1328 cm^{-1} apportioned to the C–O of syringyl derivative and 605 cm^{-1}apportioned to C–Cl.[41] While distinct bands such as 3229 cm^{-1} allocated to the N–H stretching of amine, 1410 cm^{-1} assigned to the C=C benzene ring, and 1159 cm^{-1} apportioned to the C–O vibration in lignin appeared in the spectrum for Fe_3O_4@Ap/CTAB,[42] a band at 1117 cm^{-1} assigned to C–N stretching also appeared. It is worth noting that in the spectrum for Fe_3O_4@Ap/CTAB new bands at 570 cm^{-1} and 456 cm^{-1} emerged, ascribed to Fe–O bonds in the Fe_3O_4@Ap/CTAB. Similar trends were earlier reported for metal–oxygen bonds.[43]

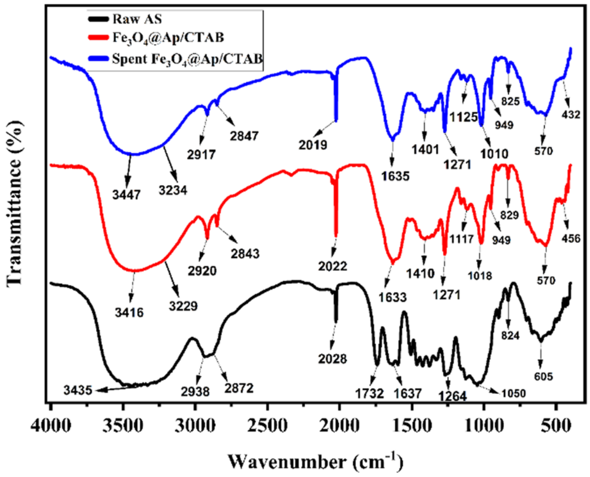

Fig. 1 FTIR spectra of raw AS, Fe_3O_4@Ap/CTAB and the spent adsorbent.

X-ray diffraction (XRD)

The diffraction patterns of raw AS, Fe_3O_4@Ap/CTAB composite and the spent nanocomposite are presented in Fig. 2. The non-crystalline attribute of the raw AS was established by the broad peaks, which appeared at 2θ values of 21.27°, 34.60° and 39.45° in its pattern.[44] The major peaks of the Fe_3O_4@Ap/CTAB nanocomposite appeared at 2θ values of 18.24°, 30.13°, 35.47°, 43.16°, 53.59°, 57.10°, and 62.79°, which are correspondingly indexed in the Fe_3O_4 monoclinic phase, with a space group of *Cc* (ICDD: 04-025-0335) of (202), (224), (422), (008), (624), (606), and (448). The very weak broad peaks at 21.42° and 40.81°, corresponding to (002) and (100) of a graphitic carbon plane structure,[42] were observed in the diffraction pattern of the nanocomposite, confirming the successful synthesis of the composite. Also, the diffraction pattern of the spent nanocomposite after adsorption remains the same as that of the nanocomposite before adsorption, proving that the synthesised nanocomposite adsorbent is structurally stable.

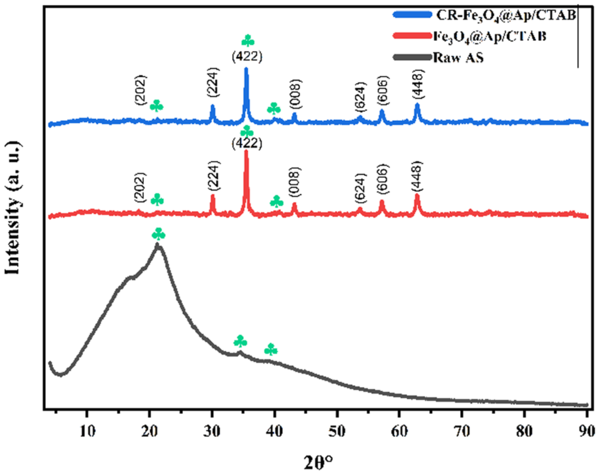

Fig. 2 XRD pattern of raw AS, Fe_3O_4@Ap/CTAB composite and the spent adsorbent.

Morphology of Fe_3O_4@Ap/CTAB

The morphology of the Fe_3O_4@Ap/CTAB nanocomposite was examined with SEM and TEM, with the results presented in Fig. 3(A–F). The surface images of the composite, Fe_3O_4@Ap/CTAB, before adsorption were observed at various magnifications: 50 μm, 10 μm, and 5 μm. Fig. 3(A) shows dark particles embedded in a perforated sheet at 50 μm magnification. At higher magnifications of 10 μm and 5 μm, Fig. 3(B) and (C), respectively, the dark particles on the perforated sheet are more clearly visible. The SEM image of the spent adsorbent in Fig. 3(D) reveals the occupation of the pores previously observed in the Fe_3O_4@Ap/CTAB nanocomposite, suggesting the CR dye adhering to the Fe_3O_4@Ap/CTAB surface. The elemental composition of Fe_3O_4@Ap/CTAB was analysed by EDX, as shown in Fig. 3(E). The presence of N, Fe and Br in the EDX of the composite, which were absent in that of the raw AS, verifies the successful synthesis of Fe_3O_4 with apricot shells and its modification with CTAB. Fig. 3(E) shows that the TEM image of Fe_3O_4@Ap/CTAB nanocomposite delivered the sheet-like clusters of AS with dark particles of Fe_3O_4 on the surface, as indicated by the yellow arrow.

Thermogravimetric analysis

The stability and performance of raw AS and Fe_3O_4@Ap/CTAB nanocomposite toward heat were evaluated using thermogravimetric analysis (TGA) in a nitrogen environment. The temperature steadily increased at 10 °C min^{-1} from 30 °C to 800 °C. Fig. 4(a and b) show the respective results. The thermogram of AS (Fig. 4(a)) depicts three significant weight loss zones within the ranges of 28 to 130 °C, 130 to 350 °C, and 350 to 613 °C. These regions correlate, respectively, to the elimination of components related to water and volatile organics, the breakdown of cellulose and hemicellulose, and the thermal oxidation of lignin. More detailed information on the nuances of heat behaviour is obtained from the DTA curves. The AS showed marked stability beginning from 613 °C.[41,42] Similarly, three weight loss zones were also visible in the Fe_3O_4@Ap/CTAB nanocomposite thermogram (Fig. 4(b)). Removal of organic compounds and water molecules was observed at 30 to 150 °C, whereas the reduction in weight at 150 to 337 °C could be ascribed to the breakdown of significant carbonisation. The Fe–O structural breakdown in the Fe_3O_4@Ap/CTAB nanocomposite was attributed to the loss at 337 to 470 °C. The Fe_3O_4@Ap/CTAB showed improved thermal stability over 470 °C with very little weight loss.[42]

Brunauer–Emmett–Teller (BET) analysis

The isotherms for nitrogen adsorption and desorption with BET analysis were utilised to determine the precise surface areas, pore capacity, and pore width of raw AS and Fe_3O_4@Ap/CTAB, as shown in Fig. 5(a). The dimensions of the surfaces of raw AS and Fe_3O_4@Ap/CTAB were 2.1019 m^2 g^{-1} and 18.7842 m^2 g^{-1}, respectively, whereas the volumes of the pore were 0.011959 cm^3 g^{-1} and 0.089736 cm^3 g^{-1}, respectively. The pore size distributions of raw AS and Fe_3O_4@Ap/CTAB were 22.7582 nm and 19.1088 nm, respectively. The Fe_3O_4@Ap/CTAB nanocomposite exhibited a significantly higher surface area (approximately 9 times larger), a smaller pore size, and a larger pore volume than raw AS. The higher surface area of the Fe_3O_4@Ap/CTAB showed a better prospective adsorption capability than raw AS. The mesoporous nature of both the raw AS and the composite is indicated by their pore diameters, which range from >2 nm to <50 nm materials.[43]

Adsorption of CR

Dosage study. The dosage of sorbent used is vital to the process's performance. The influence of Fe_3O_4@Ap/CTAB dosage (10–100 mg) on the adsorption of CR from water was examined without pH adjustment (natural pH of CR solution = 6.5) at 25 °C, 180 rpm shaking speed, 4 hours contact time in 0.05 L of 20 mg L^{-1} initial CR concentration. The result is shown in Fig. 6(a). When the amount of Fe_3O_4@Ap/CTAB was raised from 0.01 g to 0.05 g, the % removal was elevated considerably from 38.73% to 99.02%. Nevertheless, the % removal remains constant with additional dosage increases.[45] The corresponding rise in CR removal with increasing Fe_3O_4@Ap/CTAB dosage could be accounted for by the increased quantity of sorption sites and the richly active and available binding locations on the Fe_3O_4@Ap/CTAB surface.[6,46]

Contact time study

The influence of agitation or contact time (1–300 minutes) on the adsorptive removal of CR from water onto Fe_3O_4@Ap/CTAB was determined at 25 °C, 180 rpm shaking speed, pH 6.5 and 50 mg dosage in 50 mL of 20 mg L^{-1} initial CR concentration. The obtained result is presented in Fig. 6(b). As the contact time increased, the adsorption efficiency initially improved; however, this trend eventually levelled off as the reaction tended towards equilibrium. Once equilibrium was attained, there were no further gradual changes in the adsorption rate. The results indicated that 58.67% of CR was removed within 10 minutes, and an effective equilibrium, with 99.11% removal, was reached after 240 minutes. As the Fe_3O_4@Ap/CTAB nanocomposite's empty sites become fewer, its initial

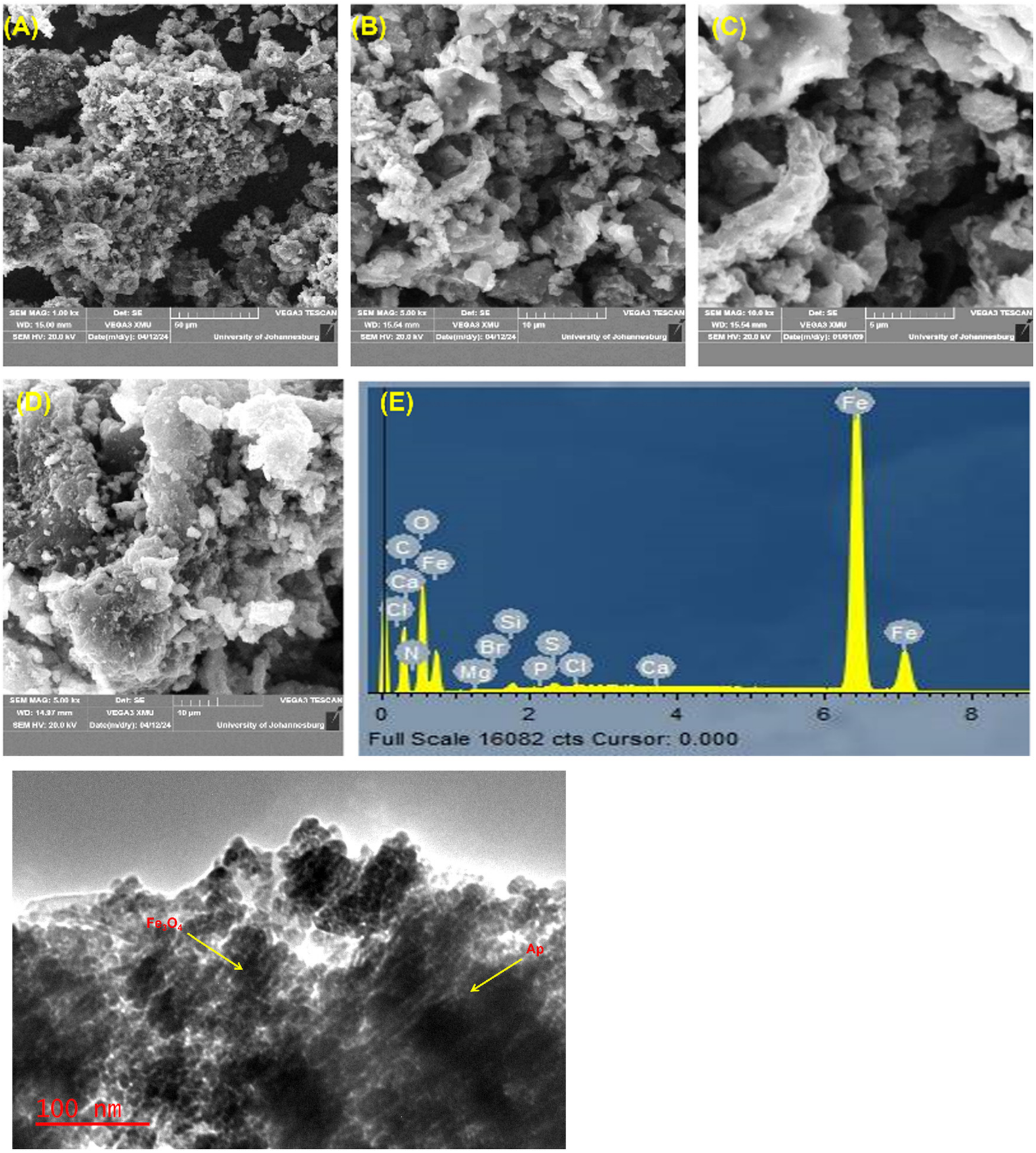

Fig. 3 SEM image of Fe_3O_4@Ap/CTAB before adsorption at (A) 50 μm, (B) 10 μm, and (C) 5 μm magnifications, and (D) after adsorption at 10 μm. (E) EDX spectra of Fe_3O_4@Ap/CTAB. (F) TEM image of Fe_3O_4@Ap/CTAB before adsorption.

capacity to enhance CR removal diminishes as the process progresses.[47]

pH studies

The interplay between the charged Fe_3O_4@Ap/CTAB surface, the ionised CR molecules, and the rate and sorption efficiency of CR from water are all greatly impacted by the solution's pH. In general, there are differences in the protonation of the groups on the surface of the adsorbent at various pH stages. Increased protonation of the adsorbent's functional groups is typically the outcome of lower pH levels.[48] The impact of the CR solution's pH (1–11) was investigated at 25 °C, 50 mg Fe_3O_4@Ap/CTAB dosage, 180 rpm shaking speed, 4 hours contact time and 20 mg L^{-1} CR concentration. The result is presented in Fig. 6(c). From the study, there was complete removal (100%) of CR at a very acidic pH region (pH $\leq$ 5) and about 98% removal was observed as the pH of the reaction medium approached the point of zero charge (pH_{pzc} = 8.04, as shown in Fig. 5(b)). The surface of the adsorbent is positively charged when the pH $<$ pH_{pzc}, while the surface carries negative charges when the pH exceeds the pH_{pzc}. This explains the decline in the percentage removal to 91%, which was observed as the pH increased from 9–11. CR dissociates into its ionic form in an acidic environment, and the colour of the solution changes from red to blue. At pH values $<$ 5, CR assumes a blue colour while it retains its red colour at pH $>$ 5. As a result, CR can bind to the

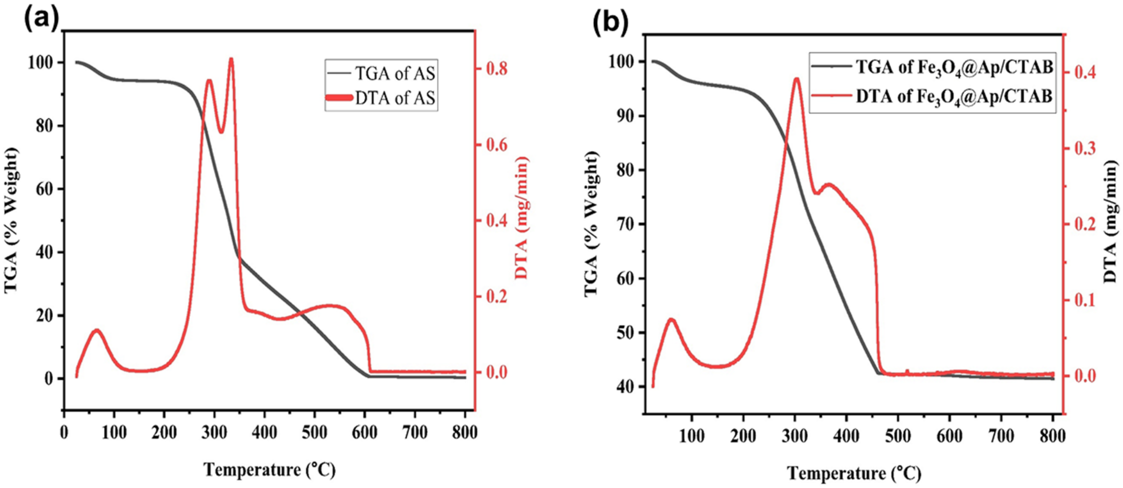

Fig. 4 TGA and DTA of (a) raw AS and (b) Fe_3O_4@Ap/CTAB.

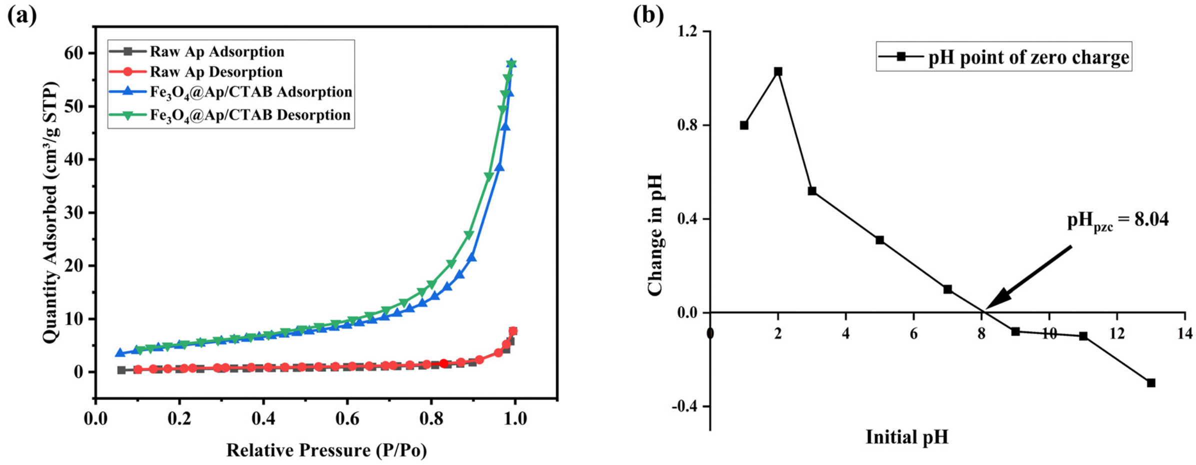

Fig. 5 (a) BET Adsorption–desorption isotherm of raw As and Fe_3O_4@Ap/CTAB nanocomposite; (b) pH point of zero charge.

adsorbent by chemically interacting with the positively charged heads of the CTAB in Fe_3O_4@Ap/CTAB through its anionic group ($-SO_3$).[49] The adsorption efficiency increased in acidic pH because of the strong interactions between H^+ and CR, as well as the attraction between the positive sorbent surface and CR. However, with the pH rising from 9 to 11, the effectiveness of Fe_3O_4@Ap/CTAB towards CR diminishes. This trend can be attributed to heightened electrostatic repulsion between the negatively charged adsorbent's surface in alkaline conditions and the negatively charged dye. Also, surplus OH^- ions compete with CR ions for the existing positively charged adsorption sites.[45] Conversely, the pH had little effect on the efficiency of CR adsorption on Fe_3O_4@Ap/CTAB, as there was 98% to 100% removal of the dye from a pH of 1 to 9. This implies that the adsorbent is effective for the removal of the target pollutant in a wide range of pH values. The strong attraction through electrostatic interactions between the anionic dye and the cationic head of the CTAB, with the interactions of the van der Waals forces of the dye molecules and CTAB, could be responsible for the significant removal efficiency of CR. Comparable trends were observed by Shayesteh *et al.* in 2016.[46]

Concentration and temperature studies

The influence of initial CR concentrations (5–50 mg L^{-1}) was examined at 298 K, 308K and 318 K, and the obtained results are shown in Fig. 6(d). As the CR concentration increases from 5 to 50 mg L^{-1}, the CR absorption per starting dye concentration increases at 298 K from 5 to 37.6 mg g^{-1}, from 5 to 38.6 mg g^{-1} (at 308 K), and from 5 to 43.7 mg g^{-1} (at 318 K). The amplified driving force, reduced diffusion barrier for CR ion transfer, and increased frequency of favourable collisions between CR ions and the adsorbent surface may be responsible for this concentration-dependent improvement in adsorption capacity.[45,46] Conversely, when the initial dye concentration was elevated, the % removal of CR declined. This is because, at greater concentrations of CR, the ratio of CR to adsorbent is

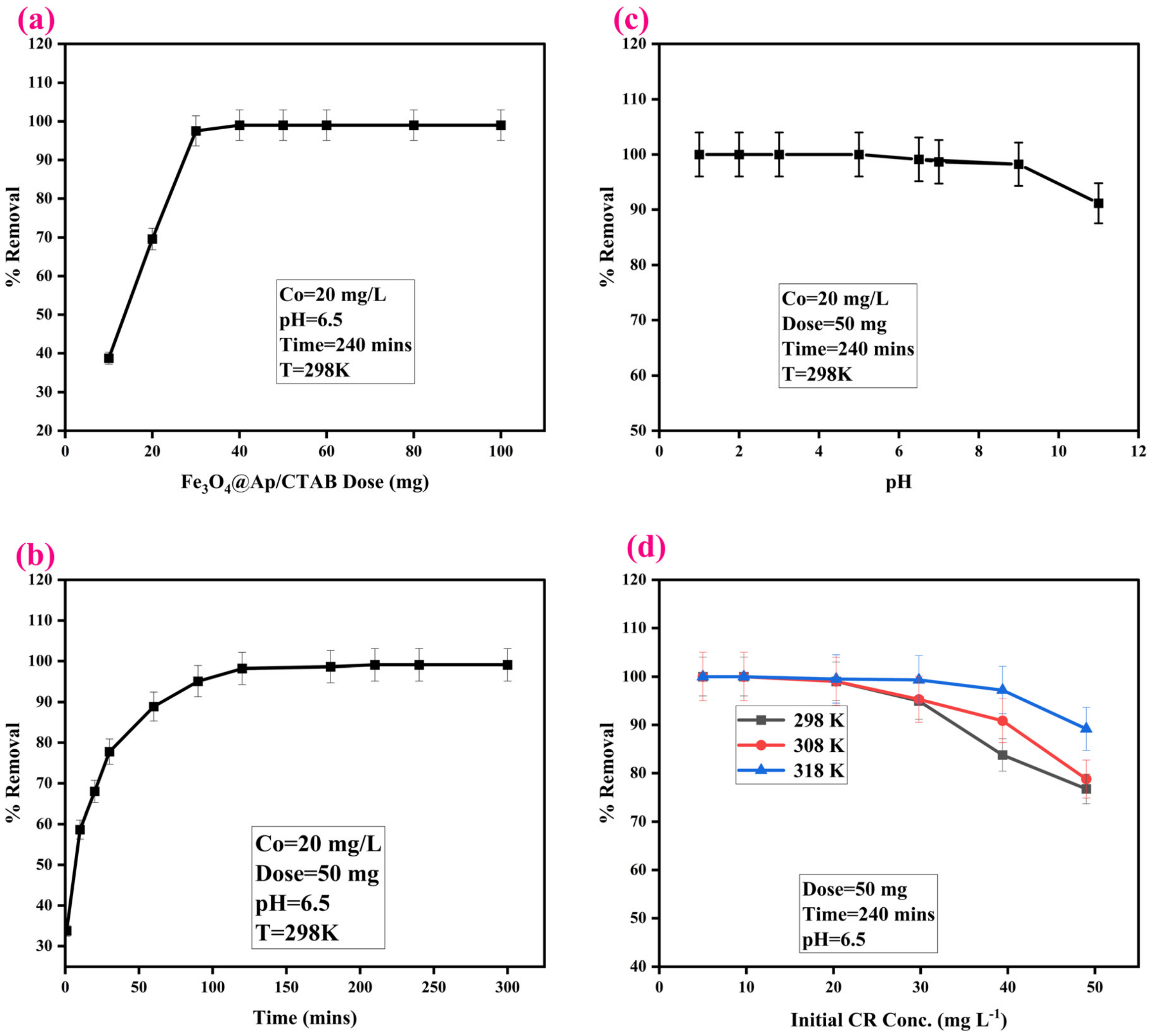

Fig. 6 (a) Dosage, (b) contact time, (c) pH, and (d) initial CR concentration studies.

bigger, which causes the adsorption sites on Fe_3O_4@Ap/CTAB to saturate more quickly. As such, CR molecules have to struggle with one another for the few active sites that are available.[50] This agrees with previous reports.[47]

Similarly, when the temperature is elevated from 298 K to 318 K, the removal efficiency also increases from 99.01% to 99.51% at 20 mg L^{-1} initial CR concentration. Thus, increasing the temperature increased the adsorption capacity from 37.175 mg g^{-1} to 44.053 mg g^{-1}. This indicates that the adsorptive removal of CR onto Fe_3O_4@Ap/CTAB is strongly influenced by temperature. Elevated temperature causes the intra- and inter-molecular H-bonds in Fe_3O_4@Ap/CTAB to weaken and break, which alters the internal structures and makes it easier for CR molecules to enter empty pores. In addition, CR molecules' average kinetic energy increases when the temperature rises from 298 K to 318 K. This accelerates their movement in the direction of the unoccupied binding sites.[43]

Equilibrium study

Using the Langmuir, Freundlich, and Temkin isotherm models, the adsorption behaviour of CR onto Fe_3O_4@Ap/CTAB was fitted and analysed. The characteristic features of the isotherm models obtained are displayed in Table 1. The monolayer adsorption of CR molecules on the uniform surface of Fe_3O_4@Ap/CTAB is described by the Langmuir isotherm. Eqn (2) expresses it in linear form.

$$\frac{C_e}{q_e} = \frac{K_L}{q_m} + \frac{1}{q_m} C_e \qquad (2)$$

where C_e represents the equilibrium concentration of CR (mg L^{-1}), q_e signifies the equilibrium amount of CR on Fe_3O_4@Ap/CTAB (mg g^{-1}), q_m denotes the maximum adsorption capacity (mg g^{-1}), and K_L stands for the Langmuir constant (L mg^{-1}).

An important Langmuir parameter is R_L, shown in eqn (3):

$$R_L = \frac{1}{1 + bC_0} \qquad (3)$$

C_0 represents the initial concentration of CR.

Adsorption is unfavourable if $R_L > 1$, exhibits linear adsorption if $R_L = 1$, is appropriate if $0 < R_L < 1$, and is irreversible if $R_L = 0$.

The Freundlich isotherm suggests that adsorption takes place on many layers. This points to the heterogeneous

Table 1 Adsorption isotherms of CR onto Fe_3O_4@Ap/CTAB

Model	Parameters	Temperature (K)		
		298	308	318
Langmuir				
	q_{max} (mg g^{-1})	37.17472	38.91051	44.05286
	K_L (L mg^{-1})	4.637931	5.354167	14.1875
	R_L	0.01051	0.009117	0.00346
	R^2	0.9943	0.9975	0.999
Freundlich				
	K_F	15.62428	16.3757	19.5254
	N	3.607504	3.430532	16.18123
	R^2	0.257	0.2297	0.0105
Temkin				
	B_T (J mol^{-1})	5.9911	6.6871	3.5156
	B	413.5421	382.9331	752.0344
	K_T (L mg^{-1})	24.65766	20.85908	1485.412
	R^2	0.4462	0.4212	0.1019

adsorption process and infinite adsorption sites with different energies on their surface. The following eqn (4) represents this.

$$\log q_e = \log K_F + \frac{1}{n}\log C_e \tag{4}$$

K_F represents the Freundlich constant, indicating the adsorption capacity (the amount of dye adsorbed) and $\frac{1}{n}$ is another Freundlich constant representing the adsorption intensity. When plotted linearly as $\log q_e$ *versus* $\log C_e$, the intercept and slope yield K_F and $\frac{1}{n}$ respectively. The parameter n represents the divergence from linearity in the adsorption process and helps determine the type of adsorption mechanism. The n values $n = 1$, $n < 1$, and $n > 1$ indicate linear, chemical, and physical adsorption processes for the adsorption systems.

The Temkin isotherm looks at the heat of adsorption between the adsorbate and adsorbent. The expressed linear form is given as eqn (5).

$$q_e = \frac{RT}{b}\ln K_t + \frac{RT}{b}\ln C_e \tag{5}$$

R is 8.314 J mol^{-1} K^{-1} (gas constant), T (K) is the operating temperature, and K_t (L g^{-1}) and b (kJ mol^{-1}) are Temkin isotherm constants that reflect maximal binding energy and heat of adsorption, respectively.

It was observed, based on the R^2 values of the three models, that the uptake of CR onto Fe_3O_4@Ap/CTAB fits best into the Langmuir model (Table 1). The Langmuir model has an R^2 value of 0.9943, contrary to the Freundlich and Temkin models, which have R^2 of 0.257 and 0.4462, respectively. The highest adsorption capacity, as determined by the Langmuir model, was 37.175 mg g^{-1} at 298 K, which was found to increase to 44.053 mg g^{-1} with temperature. This was found to be higher than and comparable to results obtained in the literature from other adsorbents. The comparison is stated in Table 2. Evident in Table 1 are the R_L values obtained from the model, which decreased as the temperature increased, and these values were within the range $0 < R_L < 1$, suggesting an appropriate and favourable CR-Fe_3O_4@Ap/CTAB adsorption process. The degree of adsorption of CR-Fe_3O_4@Ap/CTAB and the heterogeneous relationship of the process could be explained by the Freundlich model. The large K_F value (15.62428 at 298 K), which increases with increasing temperature, and the n value (3.607504) > 1 is suggestive of a strong affinity of Fe_3O_4@Ap/CTAB for CR.[1] The isotherm models' fitness to the data is Langmuir > Temkin > Freundlich.

Kinetics study

The adsorption kinetics that reveals the mechanism of CR uptake on Fe_3O_4@Ap/CTAB was investigated using four models, namely: pseudo-first-order (PFO), pseudo-second-order (PSO), Elovich and Intra-particle diffusion (IPD). The mathematical expressions of each of the models are given in eqn (6) to (9), respectively.

$$\text{PFO: } \ln(q_e - q_t) = \ln q_e - K_1\text{t}) \tag{6}$$

$$\text{PSO: } \frac{t}{q_t} = \frac{t}{q_e} + \frac{1}{K_2{q_e}^2} \tag{7}$$

$$\text{Elovich: } q_t = \frac{1}{\beta}\ln(\alpha\beta) + \frac{1}{\beta}\ln t \tag{8}$$

$$\text{IPD: } q_t = Kt^{1/2} + C \tag{9}$$

Table 2 Different adsorbents with their maximum adsorption capacities (max)

	pH	q_{max} (mg g^{-1})	Time (min)	Ref.
PVC@graphene-polyaniline	4.5	40.00	360	51
Peanut shell	8	15.1	40	52
Zeolite; Padina gymnospora/zeolite	7	9.23; 12.38	480	53
CTAB modified pumice	8	27.32	1440	46
Hollow Zn–Fe_2O_4 nanospheres	6	16.58	120	54
Apricot kernel (seed)	3–5	5.38, 5.41	50	24
Apricot stone (seed)/H_3PO_4	13	32.85, 23.42	40	23
Fly ash	Natural pH	22.12	50	55
Natural clinoptilolite	3	16.92	240	25
PANI/ZTO	Natural pH	64.51	15	49
Cashew nutshell	3	5.18	120	56
PANI/Fe_3O_4	—	21.38	90	57
Na-Bentonite; Kaolin	Neutral	35.84; 5.44	60	58
Fly ash/$NiFe_2O_4$ composites	7	22.73	180	59
Antigonon leptopus leaf	5	18.18	60	9
Water hyacinth stem & leaf	Natural pH	14.36 & 13.908	60	13
Bricks Kiln Chamber Fly Ash	4	33.3	30	60
Fe_3O_4@Ap/CTAB	**6.5**	**37.18, 44.05**	**240**	**This study**

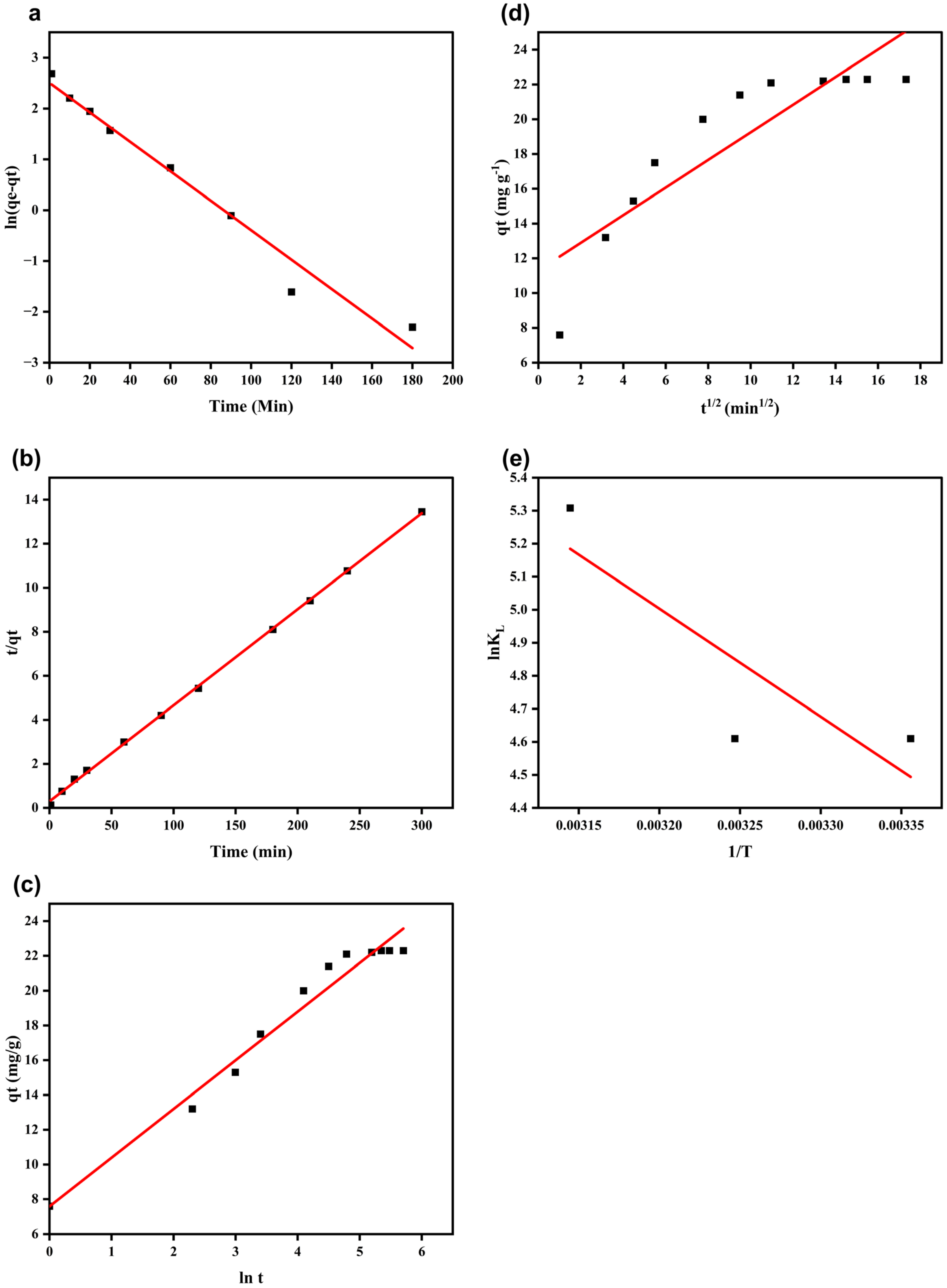

Fig. 7 (a) PFO kinetic, (b) PSO kinetic, (c) Elovich, (d) IPD, and (e) thermodynamic plots of CR adsorption.

q_e and q_t represent the quantities of adsorbed CR (mg g^{-1}) at equilibrium and at any given period of time (min), respectively, while t is time (min), K_1 (min^{-1}), K_2 (g mg^{-1} min^{-1}) and K (mg g^{-1} min$^{-1/2}$) are the rates constants of pseudo-first order (PFO), pseudo-second-order (PSO) and intraparticle diffusion models, respectively. α is the initial adsorption rate constant, and

β is the constant of desorption correlating to the energy required for chemisorption as well as surface coverage. The PFO establishes a one-order link between time change and adsorption capacity, whereas the PSO establishes a second-order relationship between adsorption capacity and concentration. This model depicts how the dye's dissolved ions adsorb onto the adsorbent surface through cation exchange or chemical sharing, with a chemical process involved. The Elovich model depicts the activated chemisorption process because it is widely correlated to chemisorption kinetics. It can handle a wide range of sluggish adsorption procedures. It is applicable to heterogeneous adsorbent surfaces. The IPD model determines the rate-controlling step for the adsorption process.

The fittings of the adsorption data into these models are shown in Fig. 7(a)–(d), and the results of the parameters obtained are displayed in Table 1. The PSO more appropriately describes the kinetics of CR adsorption onto Fe_3O_4@Ap/CTAB because it has the highest R^2 value of 0.9995 in comparison to other models, as seen in Table 1. The high closeness of the calculated ($q_{e(calc.)}$) and the experimental ($q_{e(exp.)}$) equilibrium quantities (22.94 mg L^{-1} and 22.30 mg L^{-1}, respectively) and the very low sum of square errors (SSE) of 0.212 also corroborate the better fitting of the adsorption data to PSO than PFO and other tested kinetic models. A similar trend in the uptake of CR on various materials has been published.[47,61,62]

The fitting of the adsorption data to the PSO model is a sign that the process of CR adhering to Fe_3O_4@Ap/CTAB advances by a number of mechanisms, which include attraction of the negative CR ions to the active centre of the adsorbent's surface and chemical interactions between CR and Fe_3O_4@Ap/CTAB (Table 3).[1]

Thermodynamic study

The thermodynamics of the CR-Fe_3O_4@Ap/CTAB sorption process were investigated at temperatures of 298 K, 308 K and 318 K to access the free energy, entropy and enthalpy change of the system using eqn (10)–(12). The results of these are displayed in Table 4.

$$\Delta G^0 = -RT\ln K_L \tag{10}$$

Table 3 Kinetic models of CR adsorption on Fe_3O_4@Ap/CTAB

Model	Parameter	Value
PFO	$q_{e(calc.)}$ (mg g^{-1})	12.24038
	$q_{e(exp.)}$ (mg g^{-1})	22.3
	R^2	0.97336
	K_1 (min^{-1})	0.02899
	SSE	3.353208
PSO	$q_{e(calc.)}$ (mg g^{-1})	22.93578
	$q_{e(exp.)}$ (mg g^{-1})	22.3
	R^2	0.9995
	K_2 (g mg^{-1} min)	0.006377
	SSE	0.211927
Elovich	A	42.07712
	B	0.356977
	R^2	0.9708
IPD	R^2	0.7846
	K_{diff} (mg g^{-1} $min^{-1/2}$)	0.7942
	C	11.308

Table 4 Thermodynamic parameters of CR on Fe_3O_4@Ap/CTAB

Temp. (K)	K_L (L mol^{-1})	ΔG^0 (kJ mol^{-1})	ΔH^0 (kJ mol^{-1})	ΔS^0 (kJ mol^{-1} K^{-1})
298	100.5	−11.422	+27.193	+0.129
308	100.5	−11.8053		
318	202	−14.0343		

$$\Delta G^0 = \Delta H^0 - T\Delta S^0 \tag{11}$$

$$\ln K_L = \frac{\Delta S^0}{R} - \frac{\Delta H^0}{RT} \tag{12}$$

where ΔG^0 is the standard Gibb's free energy change, ΔH^0 is the standard enthalpy change, ΔS^0 is the standard entropy change, R is the gas constant, and T is the temperature. The slope and intercept of the graph of $\ln K_L$ *versus* $\frac{1}{T}$ (Fig. 7(e)) give the values of ΔH^0 and ΔS^0, respectively.

The CR-Fe_3O_4@Ap/CTAB sorption process was feasible and spontaneous as ΔG^0 has negative values from −11.422 kJ mol^{-1} to −14.0343 kJ mol^{-1}, while both ΔS^0 and ΔH^0 have positive values of +0.129 kJ mol^{-1} K^{-1} and +27.193 kJ mol^{-1}, respectively. Furthermore, the spontaneity of the process was enhanced by the positive value of ΔS^0, which signifies an elevated degree of disorderliness in the system. The positive ΔH^0 value further proves the endothermic character of the process.

Removal of CR from a real wastewater sample

A real wastewater sample collected from the ERWART wastewater treatment plant was spiked with CR dye and was adsorbed using the nanocomposite. The initial dye concentration in the real wastewater sample prior to treatment was determined to be 7.1 ppm. The nanocomposite achieved a 95.78% removal from real wastewater after shaking for 180 minutes at 180 rpm at 25 °C under natural wastewater conditions. This shows the great potential of the sorbent for the efficient treatment of dye-containing wastewater.

Adsorption mechanism of CR with Fe_3O_4@Ap/CTAB adsorbent

In order to investigate the adsorption mechanism of CR with Fe_3O_4@Ap/CTAB adsorbent, the Congo red dye was first adsorbed on the surface of the adsorbent. This phenomenon may have been brought about by an electrostatic interaction between the positive charge surfaces of Fe_3O_4@Ap/CTAB adsorbent and the negative charge surface of CR. Furthermore, the aromatic character of CR and the Ap in the Fe_3O_4@Ap/CTAB adsorbent was also involved in a hydrophobic (π–π) interaction.[63] A schematic diagram showing the proposed mechanism of adsorption is displayed in Scheme 2.

Artificial neural network (ANN) optimal model

The best model obtained after the parameter grid search (shown in Fig. 8(a)) was found to contain the following parameters: 'tanh' activation, 0.0001 alpha value, 100 neurons in the hidden layer, constant learning rate, 'sgd' solver, iterations of 1000, and a random state of 42. This model was trained and tested on the adsorption data. The result of the ANN prediction of the adsorptive removal of CR on Fe_3O_4@Ap/CTAB and the percentage

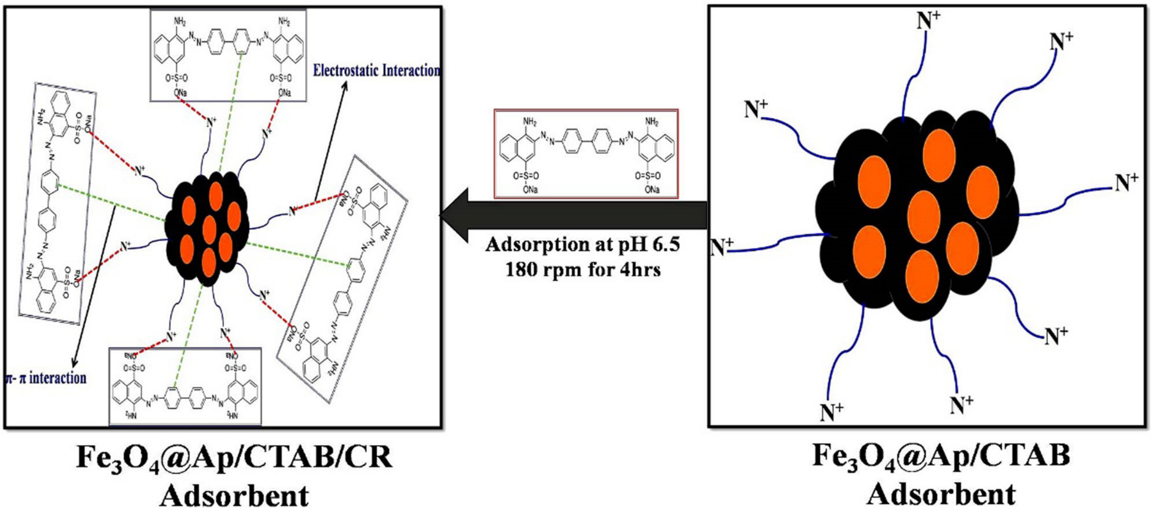

Scheme 2 Proposed adsorption mechanism.

error (determined by eqn (13)) is shown in Table 5. The prediction was then compared with the actual experimental results. The plot of the experimental values with the corresponding ANN predicted values is given in Fig. 8(b). The mean absolute error was found to be 1.7626; the mean squared error was 14.8586; the average percentage error was 0.3866, and the coefficient of determination (R^2) was 0.9587, suggesting the high prediction accuracy of the model and the great promise it carries. This ANN modelling approach has great potential as the five input variables, pH of the CR solution, agitation time, adsorbent dosage, concentration, and temperature, in the recommended ANN model are enough for the prediction of the effective sequestering of CR.

$$\%\,\text{Error} = \frac{\text{Experimental value} - \text{Predicted value}}{\text{Experimental value}} \times 100 \qquad (13)$$

Reuse and regeneration of the nanocomposite

A study of the reusability of the nanocomposite was conducted. CR was desorbed from the nanocomposites, and the composites reapplied for the adsorption in order to understand and assess its reusability. This was done as follows: 50 mg of the Fe_3O_4@Ap/CTAB nanocomposite in a 50 mL CR solution (20 mg L^{-1}) was used in the initial adsorption studies, carried out for 3 hours at 25 °C and 180 rpm. The CR-saturated Fe_3O_4@Ap/CTAB nanocomposite was then shaken for two hours with 50 mL of ethanol for a complete desorption process.[64] After that, the revitalised adsorbent was extracted with the aid of a strong magnet, cleaned with distilled water, and dried for 12 hours at 65 °C to get ready for the next adsorption/desorption cycle at the same CR concentration. Four cycles of this full process were carried out (as shown in Fig. 9), and the sorbent was 80.86% efficient for the

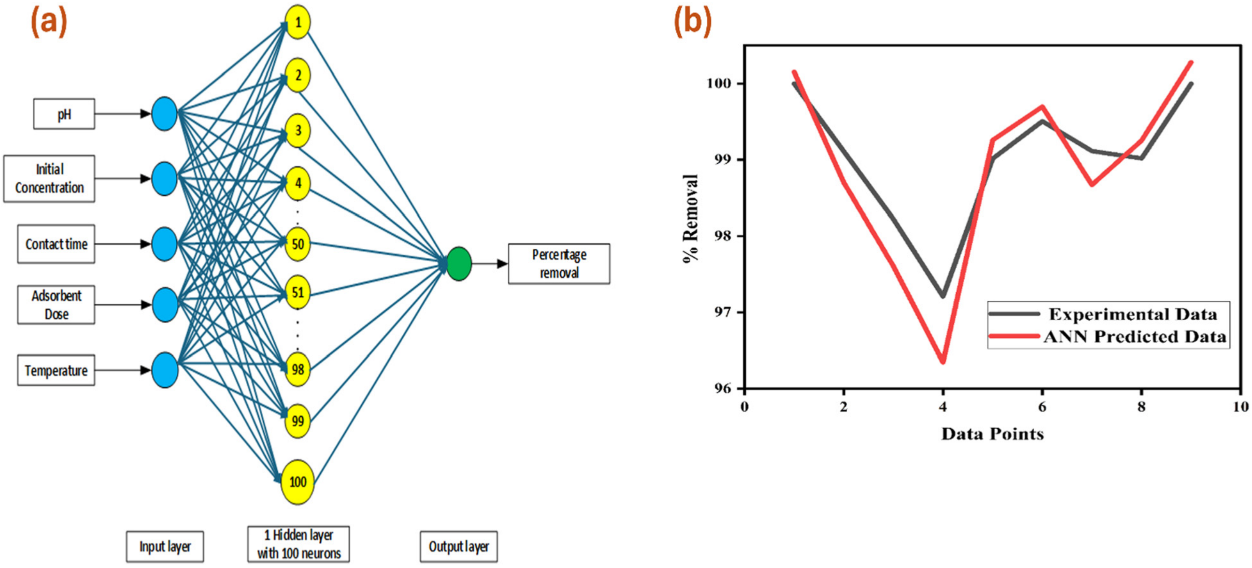

Fig. 8 (a) Architecture of the optimum model, and (b) the plot of the experimental values with the corresponding ANN predicted values.

Table 5 The ANN predicted and the experimental values of the adsorption efficiency of CR removal

pH	C_o	Time	Dose	Temp.	Experimental % removal	ANN predicted % removal	% Error
6.5	5	240	50	45	100	100.1507985	0.150799
6.5	22.5	240	50	25	99.11111	98.70220604	0.412571
6.5	22.5	120	50	25	98.22222	97.604	0.62941
6.5	39.4	240	50	45	97.20812	96.34587857	0.887006
6.5	20.3	240	50	35	99.01477833	99.2586255	0.246274
6.5	20.3	240	50	45	99.50739	99.6978142	0.191367
6.5	22.6	240	50	25	99.11504	98.67080303	0.448203
6.5	20.4	240	50	25	99.01961	99.25281397	0.235513
3	22.6	240	50	25	100	100.2781661	0.27817

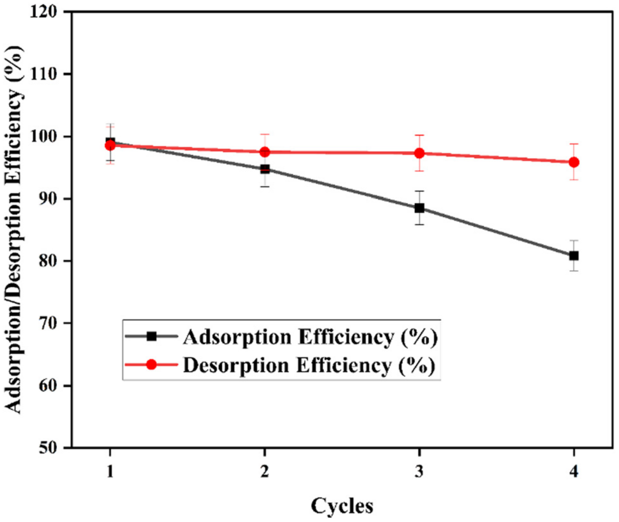

Fig. 9 Reusability cycle of the adsorbent.

removal of CR, with a desorption efficiency of 95.86% in the fourth cycle. The desorption efficiency was determined by:

$$\text{Desorption efficiency (\%)} = \frac{\text{Amount of CR desorbed}}{\text{Amount adsorbed}} \times 100 \tag{14}$$

The leaching study conducted showed 0.21 mg L^{-1} of iron after the adsorption using the composite. This is less than 0.3 mg L^{-1}, which is the recommended or permissible level of iron in drinking water given by the WHO.[65]

Conclusions

The present study successfully synthesised a novel Fe_3O_4@Ap/CTAB nanocomposite and utilised ANNs to ascertain the ideal procedure settings for eliminating CR from wastewater by using the nanocomposite as a sorbent. The best criteria for the adsorption experiment that produced the highest possible adsorption capacity value of 37.175 mg g^{-1} at room temperature and 44.053 mg g^{-1} at 45 °C were pH 6.5, 50 mg dosage, a concentration of 22.3 mg L^{-1}, and 240 minutes. The adsorption data are most accurately characterised by the Langmuir isotherm and the Pseudo second-order kinetic model. The thermodynamic investigations reveal an endothermic, favourable and spontaneous process. A multi-layer 'feed-forward neural network' comprising 5 input parameters, a hidden layer, and a single output parameter was used to forecast how much CR could be removed. Metrics, including the coefficient of regression (R^2), mean squared error, average percentage error, and mean absolute error, were used to evaluate the network's performance. With the R^2 value being 0.9587, the small relative percentage error comparing the test and predicted data suggests that the developed ANN model successfully captured the multidimensional features of CR removal efficiency. In order to remove as much CR as possible from aqueous solutions using Fe_3O_4@Ap/CTAB, this model of ANN can be employed for the prediction and optimisation of the adsorption process parameters, helping to provide pure water.

Author contributions

A. O. Akinola: conceptualisation, data curation, formal analysis, investigation, methodology, software, and writing – original draft. E. Prabakaran: methodology, project administration, and writing – review & editing. K. Govender: supervision, software, validation, visualisation, and writing – review & editing. K. Pillay: conceptualisation, supervision, funding acquisition, validation, resources, validation, and writing – review & editing.

Data availability

The Python 3.10.12 with TensorFlow version 2.15.0 code used for the ANN modelling is available at **https://drive.google.com/drive/folders/1KEMCUuj_oVTpbzJKD2WobzX7gvWIMv29?usp=sharing**.

Conflicts of interest

There are no conflicts to declare.

Acknowledgements

The authors are grateful to the Global Excellence and Stature, Fourth Industrial Revolution (GES 4.0) Initiatives and the Faculty of Science, University of Johannesburg, South Africa.

References

1 O. V. Anumasahun, A. O. Akinola, O. O. Bello, O. S. Agboola and O. S. Bello, *Chem. Data Collect.*, 2023, **44**, 100997.
2 I. Md Meftaul, K. Venkateswarlu, R. Dharmarajan, P. Annamalai and M. Megharaj, *Sci. Total Environ*, 2020, **711**, 134612.
3 Z. N. Garba, A. K. Abdullahi, A. Haruna and S. A. Gana, *Beni-Suef Univ. J. Basic Appl. Sci.*, 2021, **10**, 19.
4 O. S. Bello, F. T. Akinwale, O. S. Agboola, A. O. Ibrahim and O. O. Adesina, *Biomass Convers. Biorefin.*, 2024, **14**, 5157–5170.
5 A. Sharma, Z. M. Siddiqui, S. Dhar, P. Mehta and D. Pathania, *Sep. Sci. Technol.*, 2019, **54**, 916–929.

6 P. VenkataRao, G. SaiTarun, C. Govardhani, B. Manasa, P. Joel Joy and M. Vangalapati, *Mater. Today: Proc.*, 2020, **26**, 3009–3014.

7 W. Aktar, *Adv. Environ. Res.*, 2011, **13**(2), 423–432.

8 N. Khatri and S. Tyagi, *Front. Life Sci.*, 2015, **8**, 23–39.

9 V. Sri Devi, B. Sudhakar, K. Prasad, P. Jeremiah Sunadh and M. Krishna, *Mater. Today: Proc.*, 2020, **26**, 3197–3206.

10 P. Hadi, J. Barford and G. McKay, *J. Environ. Chem. Eng.*, 2014, **2**, 332–339.

11 S. Sumiyati, H. S. Huboyo and B. S. Ramadan, *E3S Web Conf.*, 2019, **125**, 03015.

12 Q.-S. Liu, T. Zheng, P. Wang, J.-P. Jiang and N. Li, *Chem. Eng. J.*, 2010, **157**, 348–356.

13 A. Extross, A. Waknis, C. Tagad, V. V. Gedam and P. D. Pathak, *Int. J. Environ. Sci. Technol.*, 2023, **20**, 1607–1644.

14 Y. Omidi Khaniabadi, M. J. Mohammadi, M. Shegerd, S. Sadeghi and H. Basiri, *Environ. Health Eng. Manage. J.*, 2016, **4**, 29–35.

15 S. Dawood, T. K. Sen and C. Phan, *Water, Air, Soil Pollut.*, 2014, **225**, 1818.

16 M. A. M. Salleh, D. K. Mahmoud, W. A. W. A. Karim and A. Idris, *Desalination*, 2011, **280**, 1–13.

17 B. T. Hosseinabady, P. Ziarati, E. Ballali and K. Umachandran, *J. Environ. Anal. Toxicol.*, 2018, **8**, 1–8.

18 Ş. Yüksel and R. Orhan, *Arab. J. Sci. Eng.*, 2019, **44**, 5345–5357.

19 T. D. Šoštarić, M. S. Petrović, F. T. Pastor, D. R. Lončarević, J. T. Petrović, J. V. Milojković and M. D. Stojanović, *J. Mol. Liq.*, 2018, **259**, 340–349.

20 Y. Önal, *J. Hazard. Mater.*, 2006, **137**, 1719–1728.

21 E. Demirbas, M. Kobya and M. T. Sulak, *Bioresour. Technol.*, 2008, **99**, 5368–5373.

22 S. Kahraman, P. Yalcin and H. Kahraman, *Water Environ. J.*, 2012, **26**, 399–404.

23 M. Abbas and M. Trari, *Process Saf. Environ. Prot.*, 2015, **98**, 424–436.

24 A. F. D. AL-Niaimi and F. H. Muhi, *Biochem. Cell. Arch.*, 2020, **20**, 2273–2279.

25 R. Nodehi, H. Shayesteh and A. R. Kelishami, *Microchem. J.*, 2020, **153**, 104281.

26 K. L. Bhowmik, A. Debnath, R. K. Nath, S. Das, K. K. Chattopadhyay and B. Saha, *J. Mol. Liq.*, 2016, **219**, 1010–1022.

27 S. Zhai, R. Chen, J. Liu, J. Xu and H. Jiang, *J. Taiwan Inst. Chem. Eng.*, 2021, **120**, 161–168.

28 M. Yilmaz, T. J. Al-Musawi, M. Khodadadi Saloot, A. D. Khatibi, M. Baniasadi and D. Balarak, *Biomass Convers. Biorefin.*, 2024, **14**, 649–662.

29 H.-T. Thai, *Structures*, 2022, **38**, 448–491.

30 K. Yetilmezsoy and S. Demirel, *J. Hazard. Mater.*, 2008, **153**, 1288–1300.

31 M. Tanzifi, S. H. Hosseini, A. D. Kiadehi, M. Olazar, K. Karimipour, R. Rezaiemehr and I. Ali, *J. Mol. Liq.*, 2017, **244**, 189–200.

32 N. G. Turan, B. Mesci and O. Ozgonenel, *Chem. Eng. J.*, 2011, **171**, 1091–1097.

33 N. Daneshvar, A. R. Khataee and N. Djafarzadeh, *J. Hazard. Mater.*, 2006, **137**, 1788–1795.

34 S. Ullah, M. A. Assiri, M. A. Bustam, A. G. Al-Sehemi, F. A. Abdul Kareem and A. Irfan, *Paddy Water Environ.*, 2020, **18**, 455–468.

35 K. K. Ilavenil, P. Pandian and A. Kasthuri, *Mater. Today: Proc.*, 2023, **72**, 2344–2350.

36 M. Akhond, G. Absalan and E. Rafatmah, *Anal. Bioanal. Chem. Res.*, 2016, **3**, 225–237.

37 M. H. Armbruster and J. B. Austin, *J. Am. Chem. Soc.*, 1938, **60**, 467–475.

38 V. Temkin and M. J. Pyzhev, *Ussr*, 1940, **12**, 217–225.

39 H. Freundlich, *Zeitschrift für Phys. Chemie*, 1907, **57U**, 385–470.

40 M. S. Reza, S. Afroze, M. S. A. Bakar, R. Saidur, N. Aslfattahi, J. Taweekun and A. K. Azad, *Biochar*, 2020, **2**, 239–251.

41 K. Aljoumaa, H. Tabeikh and M. Abboudi, *J. Indian Acad. Wood Sci.*, 2017, **14**, 127–132.

42 E. Prabakaran, K. Pillay and H. Brink, *Mater. Today Sustainability*, 2022, **18**, 100123.

43 O. I. Adeiga and K. Pillay, *J. Environ. Manage.*, 2024, **355**, 120274.

44 Ç. S. Özdemir, H. Varliklioz and S. Yapici, *J. Phys. Chem. Funct. Mater.*, 2018, **1**, 18–24.

45 S. Mohebali, D. Bastani and H. Shayesteh, *J. Mol. Struct.*, 2019, **1176**, 181–193.

46 H. Shayesteh, A. Rahbar-Kelishami and R. Norouzbeigi, *J. Mol. Liq.*, 2016, **221**, 1–11.

47 J. N. Wekoye, W. C. Wanyonyi, P. T. Wangila and M. K. Tonui, *Environ. Chem. Ecotoxicol.*, 2020, **2**, 24–31.

48 P. Koohi, A. Rahbar-kelishami and H. Shayesteh, *Environ. Technol. Innov.*, 2021, **23**, 101559.

49 S. Singh, S. Perween and A. Ranjan, *J. Environ. Chem. Eng.*, 2021, **9**, 105149.

50 S. K. Sahoo, J. P. Dhal and G. K. Panigrahi, *Compos. Commun.*, 2020, **22**, 100496.

51 R. Kumar, M. O. Ansari, N. Parveen, M. A. Barakat and M. H. Cho, *RSC Adv.*, 2015, **5**, 61486–61494.

52 A. Abbas, S. Murtaza, K. Shahid, M. Munir, R. Ayub and S. Akber, *Middle-East J. Sci. Res*, 2012, **11**, 828–832.

53 A. R. Dryaz, M. Shaban, H. AlMohamadi, K. A. A. Al-Ola, A. Hamd, N. K. Soliman and S. A. Ahmed, *Sci. Rep.*, 2021, **11**, 21058.

54 R. Rahimi, H. Kerdari, M. Rabbani and M. Shafiee, *Desalination*, 2011, **280**, 412–418.

55 M. Harja, G. Buema and D. Bucur, *Sci. Rep.*, 2022, **12**, 1–18.

56 P. Senthil Kumar, S. Ramalingam, C. Senthamarai, M. Niranjanaa, P. Vijayalakshmi and S. Sivanesan, *Desalination*, 2010, **261**, 52–60.

57 X. P. Teng, M. Y. K. Bryan, P. V. Chai and J. Y. Law, *Mater. Today: Proc.*, 2020, **46**, 1875–1881.

58 V. Vimonses, S. Lei, B. Jin, C. W. K. Chow and C. Saint, *Chem. Eng. J.*, 2009, **148**, 354–364.

59 S. K. Sonar, P. S. Niphadkar, S. Mayadevi and P. N. Joshi, *Mater. Chem. Phys.*, 2014, **148**, 371–379.

60 P. Govindaraj and N. Gnanavelraja, *Int. J. Appl. Eng. Res.*, 2018, **13**, 11693–11700.

61 M. Foroughi-dahr, H. Abolghasemi, M. Esmaieli, G. Nazari and B. Rasem, *Process Saf. Environ. Prot.*, 2015, **95**, 226–236.

62 N. F. Al-Harby, E. F. Albahly and N. A. Mohamed, *Polymers*, 2021, **13**, 4446.
63 A. Chowdhury, S. Kumari, A. A. Khan and S. Hussain, *J. Hazard. Mater.*, 2020, **385**, 121602.
64 A. Chowdhury, S. Kumari, A. A. Khan and S. Hussain, *J. Environ. Chem. Eng.*, 2021, **9**, 106554.
65 World Health Organization, Who/Sde/Wsh/03.04/08, 2003, **2**, 4.